crystals

MDPI

Article

Simulation of Porous Magnetite Deposits on Steam Generator Tubes in Circulating Water at 270 °C

Soon-Hyeok Jeon, Hee-Sang Shim, Ji-Min Lee, Jeoh Han and Do Haeng Hur *

Korea Atomic Energy Research Institute, 989-111 Daedeok-daero, Yuseong-gu, Daejeon 34057, Korea; junsoon@kaeri.re.kr (S.-H.J.); hshim@kaeri.re.kr (H.-S.S.); jmlee0915@kaeri.re.kr (J.-M.L.); jeohhan@kaeri.re.kr (J.H.)

* Correspondence: dhhur@kaeri.re.kr; Tel.: +82-42-868-8388; Fax: +82-42-868-8696

Received: 6 July 2020; Accepted: 12 August 2020; Published: 20 August 2020

Abstract: In the secondary side of pressurized water reactors (PWRs), the main corrosion product accumulated on the steam generator (SG) tubes is magnetite, which has a porous structure. The purpose of this work is to simulate the porous magnetite deposited to the SG tubes using a loop system. We newly developed a circulating loop system for a porous magnetite deposition test. A test section was designed as a single hydraulic flow channel, and a cartridge heater was fabricated and mounted into a commercial SG tube to provide an equal heating source for the primary water. After the deposition test, the simulated magnetite deposits were characterized for comparison to real SG tube deposits collected from an operating PWR plant. The magnetite deposits produced using the loop system were appropriate for simulating the real SG tube deposits because the particle characteristics, phase, and porous morphology are closely similar to those of real deposit samples. Using the loop system, the chemical impurities such as Na and Cl can be easily concentrated within the pores of the simulated magnetite deposits. These simulated magnetite samples are expected to be widely utilized in various research fields such as the heat transfer degradation and magnetite accelerated corrosion of SG tubes.

Keywords: magnetite; steam generator; sludge; loop system; simulation; nuclear power plant

1. Introduction

In the secondary coolant system of pressurized water reactors (PWRs), carbon steel, which exists in large numbers of pipings (i.e., feed-water lines, condensate components, separator drains, and heater drain systems) of steam generators (SGs), is greatly affected by the flow accelerated corrosion [1]. During the flow accelerated corrosion, carbon steel piping is oxidized to magnetite under the alkalized reducing conditions of PWRs. Afterwards, some parts of magnetite formed on carbon steel piping are removed and transported into the SGs and continuously accumulated on the secondary side of SG heat exchanger tubes, tube support plates (TSPs), and tops of tube sheets, thereby deteriorating the integrity of SGs [2,3].

There are some problems with SG integrity owing to the magnetite deposition on the SG tubes. First, the magnetite deposited on the secondary side of SG tubes causes the increase of the thermal resistance of the SG tube, which consequently decreases the heat transfer capability of SG because the magnetite that has a porous structure has a much lower thermal conductivity than the SG tubes [3]. Second, the TSP made of stainless steel may cause the deposition of magnetite at the inlet of the TSP flow path hole, which is called the TSP blockage phenomenon [4]. Figure 1 shows the secondary flow path between the SG tubes and their support plates and the TSP blockage. TSP blockage induces the high velocity regions and transverse velocities in the secondary water flow, which causes flow-induced vibrations and SG tube cracks. It also decreases the circulation ratio of the SGs [4]. In addition,

aggressive impurities such as chloride (Cl^-) and sulfate (SO_4^{2-}) ions from the make-up water, auxiliary feed-water, and condenser leakage circulate in the secondary flow to the SGs [5–7]. Afterwards, the chemical impurities are concentrated in the micro-pores of magnetite deposits [5–7], thus inducing the corrosion acceleration of SG tubes [8–10] owing to the formation of severe corrosive environments.

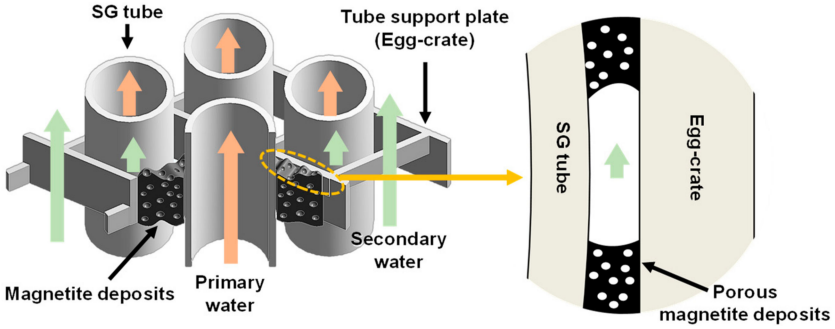

Figure 1. Schematic of the secondary flow path between the steam generator (SG) tube and their support plat and tube support plate (TSP) blockage owing to the magnetite deposits.

To prevent these problems owing to SG deposits, chemical [11] or mechanical cleanings [12] and high pH water treatment [13] of the secondary circuit have been developed and are widely used in the PWRs. Among them, chemical cleaning is currently the most effective strategy for removing the corrosion products in SGs. However, chemical cleaning is difficult to perform and could damage some parts of the SG owing to the corrosive properties of the chemical cleaning solution [4,12]. Hence, it is of great interest to investigate alternative strategies to reduce the SG fouling and TSP blockage. To study the magnetite removal method and dissolution behavior of the magnetite deposits, a suitable porous magnetite specimen deposited onto SG tubes should be provided for the researchers.

Recently, some researchers have studied the deposition of corrosion products on the nuclear tubing materials using the loop systems in PWRs. In primary water of PWRs, the deposition of unwanted products on the surface of fuel cladding tubes in the reactor core is known under the acronym of corrosion-related unidentified deposit, CRUD [14]. Fuel CRUD mainly consists of nickel ferrite ($Ni_xFe_{3-x}O_4$), nickel oxide (NiO), iron oxide (Fe_3O_4), zirconium oxide (ZrO_2), and bonaccordite (Ni_2FeBO_5) [15–17]. Nishimura et al. [18] studied the effect of dissolved hydrogen transition on the nickel deposition of the fuel cladding under simulated primary water conditions. Baek et al. [19–21] elucidated the effect of surface properties, heat flux, and hydrogen of the fuel CRUD deposition on the Zr-based alloy tubes in the primary loop system. In particular, a crud deposition test was performed using an internal rod-type heater in order to provide the condition of the sub cooled nucleate boiling (SNB) [19–21]. In the secondary side of the PWR, magnetite is mainly composed of SG tube deposits. However, the trace amount of other phases such as trevorite (Ni_2FeO_4), jacobsite (Mn_2FeO_4), chromite ($FeCr_2O_4$), and metallic Cu and Pb particles may also constitute the SG tube deposits [22,23]. Recently, Electricité de France simulated the SG tube fouling using the experimental loop called FORTRAND [24]. In this loop, the magnetite and soluble iron were formed by the corrosion of carbon steel pipes in the feedwater circuit and released in the secondary coolant [24]. Afterwards, the corrosion products were transported into the test section, where their precipitation and deposition on heated Alloy 600 TT tubes led to fouling [24].

However, the SG deposits produced using FORTRAND were composed of a dense layer of polyhedral magnetite particles (>1 μm). In addition, the small pores between the magnetite particles were also difficult to observe. Meanwhile, the real SG tube deposits of SG in operation had a porous structure, and many pores existed between the magnetite particles. For these reasons, we think that it is necessary to produce a porous SG deposit specimen for conducting porous magnetite-related studies. However, it is not necessary to form trevorite, jacobsite, and chromite because the amount of these phases is too small for studying the deposition behavior of SG tube deposits and does not always exist.

Hence, the purpose of this work is to produce a porous magnetite that can be deposited on SG tubes using a loop system. Our group newly developed a recirculating loop system for magnetite deposition tests. After performing the deposition tests, the simulated deposit samples were characterized using various analysis techniques. In addition, the real SG tube flakes were collected from the SG of the PWR in operation and were characterized in order to compare with the magnetite deposits simulated using the loop system. Moreover, the concentration factors of Na and Cl within the deposits were evaluated and compared with previously reported ones.

2. Materials and Methods

2.1. Specimen Preparation and Test Solution

Commercial Alloy 690TT tubes, which are widely used as PWR SG tubes, were selected as the test specimens. The test tubes have an outer diameter (OD) of 19.05 mm, an inner diameter (ID) of 17.00 mm, a thickness of 1.025 mm, and a total length of 500 mm. The chemical composition of the Alloy 690TT is given in Table 1.

Table 1. Chemical composition of Alloy 690TT tubes (wt.%).

Ni	Cr	Fe	C	Si	Mn	Ti	Al	Cu	Co
Bal.	29.3	10.4	0.02	0.3	0.3	0.3	0.2	0.01	0.01

One side of the tube was welded with a cap made out of a commercial Alloy 600 rod to prevent the water leaking into the tube. Afterwards, a cartridge heater of 600 mm length was mounted into the test tube to provide the heat source onto the inner surface of the tube, which was simulated as the primary coolant water. As shown in Figure 2, the cartridge heater was composed of a thermocouple, a thermocouple wire, an Ni-Cr wire, magdenesium oxide, and a sheath made of stainless steel 316. During the mounting of the heater into the tube, magnesium oxide was used to thinly cover the surface of the cartridge heater to increase the heat transfer in the circular gap between the tube and cartridge heater. The heater-mounted SG tubes were dried in an oven at 60 °C for 10 h. After the drying process, the outer surface of the SG tube specimens was cleaned using acetone.

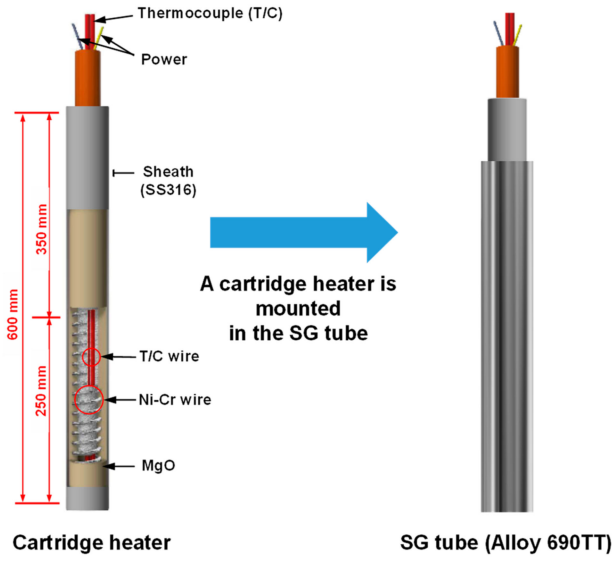

Figure 2. Design of cartridge heater and heater-mounted SG tube.

The secondary coolant water of pH 9.0 at 25 °C was used in this work. The pH of the test solution was controlled using ethanolamine, which is an organic chemical agent widely used to adjust the pH

value of the secondary side in PWR [25]. During the magnetite deposition test, the pH value was continuously monitored using in situ and ex situ pH sensors. Fe(II)-acetate was used as the precursor. It was reported that Fe(II)-acetate [26] and Fe(III)-acetate [27] were widely used to synthesize iron oxide particles. Especially, pure nanometer-sized could be simply synthesized by Fe(II)-acetate in water under an argon atmosphere [26]. Fe(III)-EDTA (ethylenediaminetetraacetic acid) or EDTA ferric sodium salt were also used to make magnetite [28,29]. However, in the Fe-EDTA forms, the undesirable other elements such as N and Na additionally existed. Furthermore, as the Fe-EDTA form is a chelating agent having a large molecular weight, a large amount of other elements must be present in the experimental solutions to set the same concentration of Fe ions. In the primary system of PWRs, acetate has been widely injected in the form of depleted zinc acetate to improve the integrity of fuel cladding and SG [30]. For these reasons, it was decided to use the Fe(II)-acetate form in this work.

The test solution containing a 260 ppm Fe source was stored in a 50 L tank for injection into the test section. The Fe-acetate solution was injected directly into the inlet part of the test section at a flow rate of 1 mL/min when the loop system was finally stabilized. The concentration of the Fe source in the test section was maintained at 1 ppm during the magnetite deposition test.

In order to evaluate the concentration behavior of chemical impurities in pores of simulated magnetite deposits, Na and Cl ions were continuously injected with the Fe source into the test section at 0.1 and 0.15 ppm concentration, respectively, during the deposition test.

2.2. Deposition Loop System

After the drying and cleaning process of the SG tube, the SG tube was then installed into the test section (Figure 3a). As shown in Figure 3b, the flow path area was designed by considering the single flow path area of the free span of the SG tube of OPR1000 from the first standard PWR plant in the Republic of Korea. The distance between both centers of the SG tubes was 24.5 mm, which is the size of a single flow path diameter including one SG tube, and the outer diameter of the SG tube was 19.05 mm, which was considered in the design of the test section.

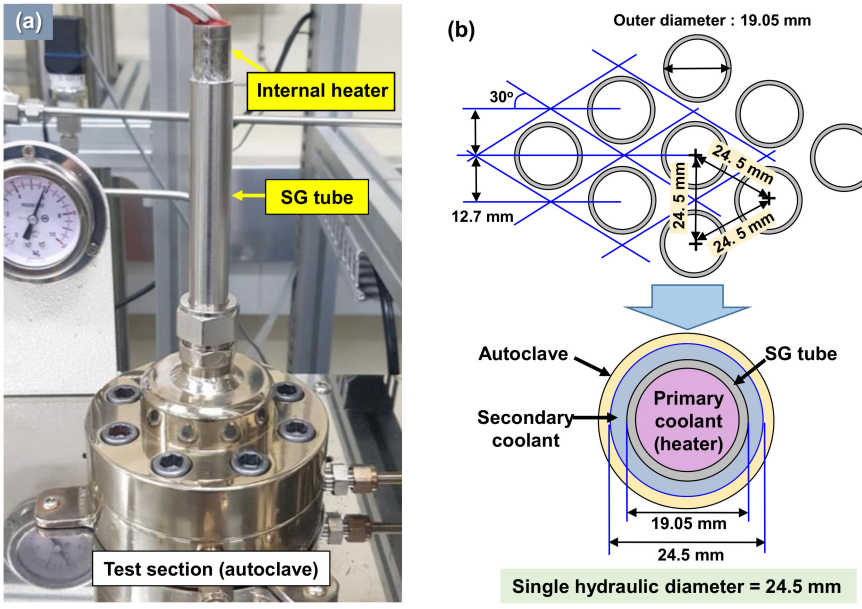

Figure 3. (**a**) Test section and internal heater-mounted SG tube and (**b**) design of test section as the single hydraulic flow channel.

Figure 4 presents a schematic of the secondary loop system for the magnetite deposition test. The recirculating loop system consists of the following main components: a simulated secondary water solution tank; an Fe source tank filled with Fe(II)-acetate solution; a high pressure (HP) diaphragm pump; a preheater for control the temperature of inlet solution; a metering pump for Fe source

injection; a heat exchanger for cooling water; a back pressure regulator (BPR) for pressure control; various water chemistry sensors for dissolved oxygen (DO), pH, and conductivity; a test section installed with a heater-mounted SG tube specimen; and a temperature controller. The water chemistry parameters, pressure, and temperature at various positions in the test section were monitored in the temperature controller using digital gauges. In order to start the deposition test, the pressure of the test section was slowly increased to 60 bar using the back pressure regulator, and the temperature of simulated secondary water near the surface of SG tube was continuously maintained at 270 °C to keep the SNB conditions by operating the pre-heater, line heater, ceramic heaters surrounding the test section, and cartridge heater inside the SG tube specimen. The heat flux of the cartridge heater was maintained at 30 W/cm^2. The flow rate adjacent to the SG tube was continuously controlled at flow rate of 260 mL/min, and the dissolved oxygen concentration was maintained below 5 ppb, which is a typical water chemistry guideline of the Electric Power Research Institute [25]. Water chemistry parameters for affecting the corrosion behavior of secondary system are pH, dissolved oxygen concentration, temperature, and concentration of various impurities (Fe, Na, Cl, S, and Si) [25]. Electric Power Research Institute water chemistry programs have been established for operating PWRs to minimize corrosion problems and, thereby, to maximize the reliability of the secondary system [25]. Under the stabilization of dissolved oxygen concentration, temperature, and pH value, the magnetite deposition test was performed for 14 days. Each deposition test was performed at least two times for reproducibility. Table 2 summarizes the main experimental conditions for the magnetite deposition tests.

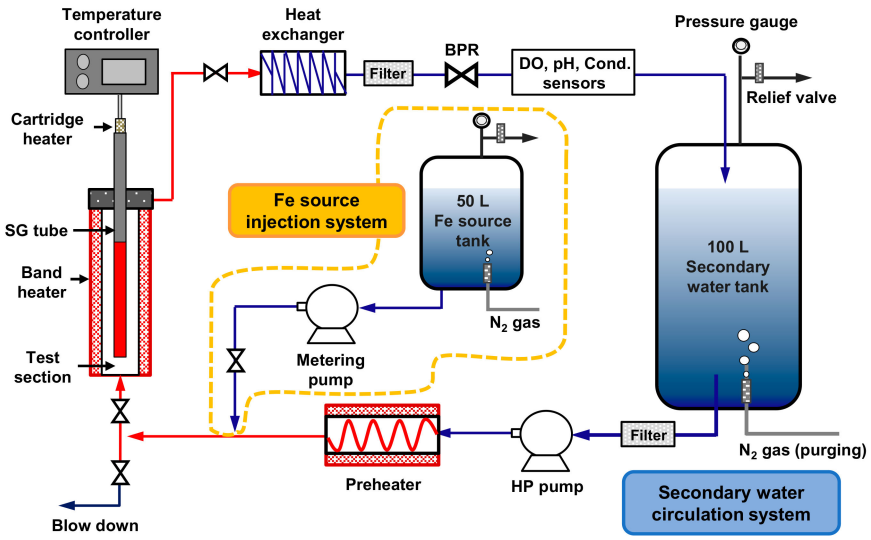

Figure 4. A schematic of the circulation secondary loop system for magnetite deposition test.

Table 2. Main conditions for the magnetite deposition tests.

Internal Heater Heat Flux	Fe Concentration at Test Section	Temperature	System Pressure	Dissolved Oxygen	pH at 25 °C	Flow Rate	Test Time
30 W/cm^2	1.0 ppm	270 °C	60 bar	<5 ppb	9.0	260 mL/min	14 days

Figure 5 shows the SG tube specimens before and after the deposition test. After the test, the outer surface of the specimen was totally covered with black-colored deposits. After the test was finished, the specimen was dried at 60 °C for about 3 h and then cut with a tube cutter. The particle morphologies on the surface of deposits were observed by a scanning electron microscope (SEM) at least three positions per specimen. The particle size, aspect ratio, and particle size distribution of both deposits were analyzed from 320 randomly selected particles on the surface SEM images. Three images per position, at least nine images per specimen, were analyzed. The aspect ratio is defined as the ratio of

the largest axis to the smallest axis of a particle, which means the shape of the particle. The closer the aspect ratio is to 1, the more circular the particle shape.

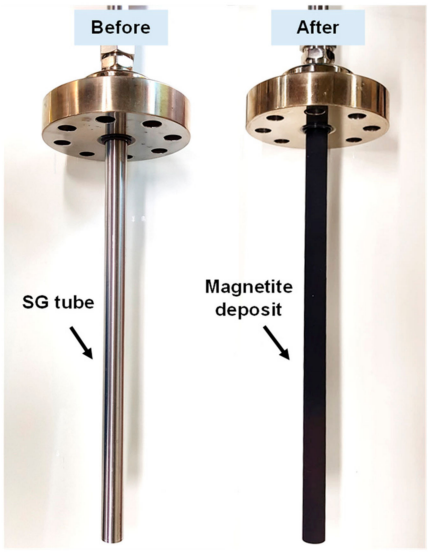

Figure 5. Photo of SG tube (Alloy 690TT) before and after the magnetite deposition test.

The focused ion beam (FIB) technique was used to observe the cross section of deposits closely. The chemical composition of the deposits was analyzed by FIB-SEM attached with an energy dispersive X-ray spectrometer (EDS) with an acceleration voltage and resolution of 10 kV and 125 eV, respectively. The phase of the deposits was analyzed by a high-resolution X-ray diffractometer (HR-XRD). The FIB milling technique was also used to fabricate the transmission electron microscope (TEM) to characterize impurity concentration within the pores of deposits. The average two-dimensional porosity of deposits was evaluated using at least eight cross-sectional SEM images by using an image analyzer (Image-Pro Plus 7.0, Media Cybernetics, Rockville, MD, USA).

To evaluate the amount of simulated deposits, two tubular specimens of approximately 20 mm in length at different axial locations per test (total four tubular samples) were immersed separately in a chemical cleaning solution (20 wt.% ethylenediaminetetraacetic acid + 1 wt.% N_2H_4 + 1 wt.% corrosion inhibitor + NH_4OH) at 93 °C for 12 h to selectively dissolve the deposits only. The cleaning solution was then subjected to an inductively coupled plasma atomic emission spectroscopy (ICP-AES) using a Thermo Scientific iCAP 7000 (Thermo Scientific, Cambridge, UK) series to measure Fe concentration, with an uncertainty of 2%. Finally, the total amount of deposits per unit area was converted to identified phases using the measured Fe concentration.

The zeta potentials of magnetite nanoparticles and Alloy 690TT surfaces were measured using a Malvern Zetasizer Nano ZS90 system (Malvern Panalytical Ltd., UK) equipped with a surface zeta potential cell kit. Magnetite nanoparticles with an average size of 5 nm were diluted to be a concentration of 5 mg/L in the same simulated secondary coolant water as that used in the magnetite deposition tests. The surface zeta potentials of the Alloy 690TT tubes were measured using the Malvern surface zeta potential cell kit. We prepared rectangular samples no larger than 7 mm × 4 mm × 1 mm. The surface roughness of the flat samples was controlled to about 0.25 μm, similar to that of the specimen used in the deposition test because the metal surface greatly affects the surface zeta potential. A flat sample was mounted on the surface zeta potential kit and immersed in a solution containing tracer magnetite nanoparticles. This solution was also the same as that used for the zeta potential measurement of the magnetite nanoparticles. The apparent tracer mobility was measured at four different distances from the sample surface through a stepwise increase of 125 μm per step. The surface zeta potential of Alloy 690TT could be calculated by a linear extrapolation. Each measurement was performed at room temperature and repeated at least three times for reproducibility. Good reproducibility was confirmed.

For comparison with the simulated magnetite deposited on an SG tube, real SG tube flake samples were provided from an operating PWR in the Republic of Korea. The flake samples were collected from the outer surface of the Alloy 600TT tubes after operating cycle 27 of a Westinghouse model-F SG during the lancing process. Before characterizing the flake samples, the samples were dried and stored in a vacuum desiccator to prevent the oxidation reactions in atmosphere. To observe the cross-sectional view of the flake samples, the samples were ion-milled using an FIB directed vertically toward the deposit layers and examined using SEM. In addition, the phase fraction of the SG flake samples was also analyzed by SEM combined with electron back-scatter diffraction (EBSD) using a Nordlys detector and Channel5 software, with an accelerating voltage and specimen tilt angle of 20 kV and 70°, respectively.

3. Results and Discussion

3.1. Morphology and Porosity of Simulated Magnetite Deposits and Samples of Real SG Flakes

Figure 6 shows the SEM images on the water side of the real SG tube flakes and simulated magnetite deposits. As shown in Figure 6a,b, for the two samples, round and polyhedral particles of sizes in the range of about 50 nm~3 μm with numerous small pores were observed. Figure 6c,d shows large pores between the particles existing on the water side of the real SG tube flakes and simulated magnetite. The large pores with a diameter between about 6 and 8 μm were considered to be associated with steam chimneys or bubble growth.

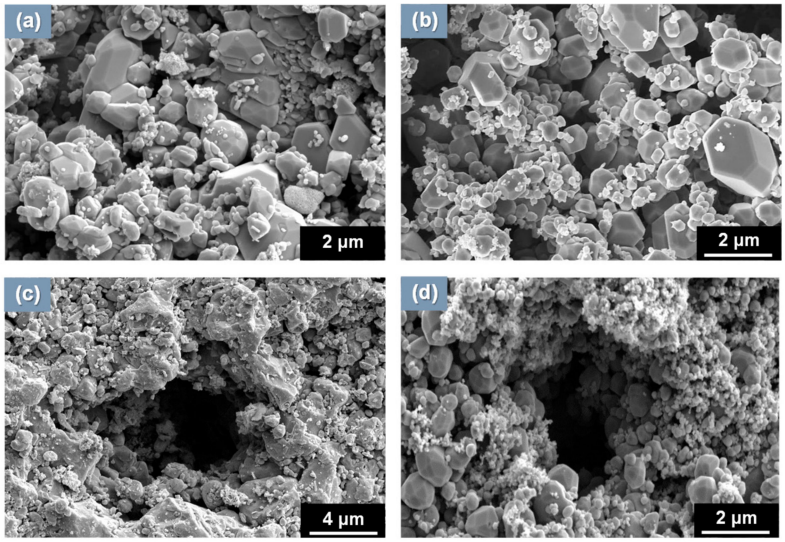

Figure 6. Scanning electron microscope (SEM) image of the outer surface of real SG tube deposits and simulated magnetite deposits: (**a**) particles of real deposits and (**b**) particles of simulated deposits, (**c**) pores of real deposits, and (**d**) pores of simulated deposits.

Figure 7 presents the particle characteristics such as mean size, aspect ratio, and size distribution. As shown in Figure 7a, the mean diameter of the simulated deposit particles was relatively larger than that of real flakes, but the distribution range is almost similar. The aspect ratio of the simulated deposit particles was nearly same as that of the real deposit particles (Figure 7b). The simulated deposit particles and real SG deposit particles with diameters ranging from 0.3 μm to 1.2 μm constitute 81% and 89%, respectively (Figure 7c). On the basis of these results, we think that the simulated deposits were appropriate to simulate the real SG tube deposits from the viewpoint of particle size and morphology.

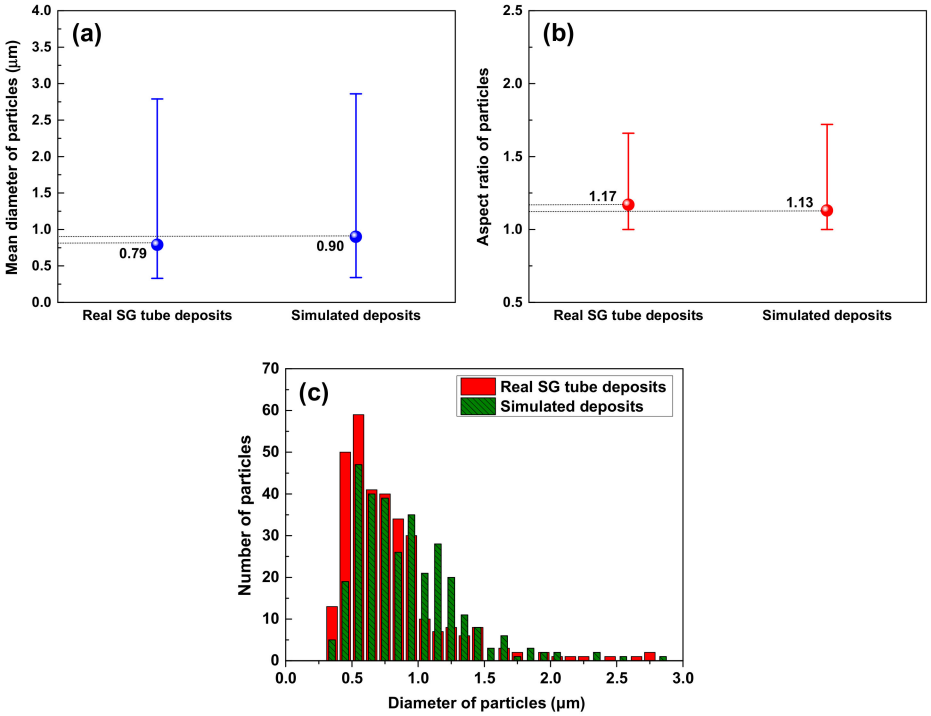

Figure 7. Particle size parameters of 320 randomly selected magnetite particles using an image analyzer: (**a**) mean diameter, (**b**) aspect ratio, and (**c**) particle size distribution.

Figure 8 shows the SEM micrographs of the cross section of the real flakes and simulated deposits. The average thickness of the flakes was about 116 μm. However, the thickness of the simulated deposits was about 15 μm, much thinner than that of the flakes. This is because the deposition time was too small, even though the test was performed under a high concentration of Fe ion sources. However, the thickness of the simulated deposits could be easily made thicker by increasing the test time. In addition, a large number of the micro-pores were observed throughout the entire surface of both samples. Although the thickness of the simulated magnetite deposits was thinner than that of the real SG tube deposits, the porous structure was well simulated.

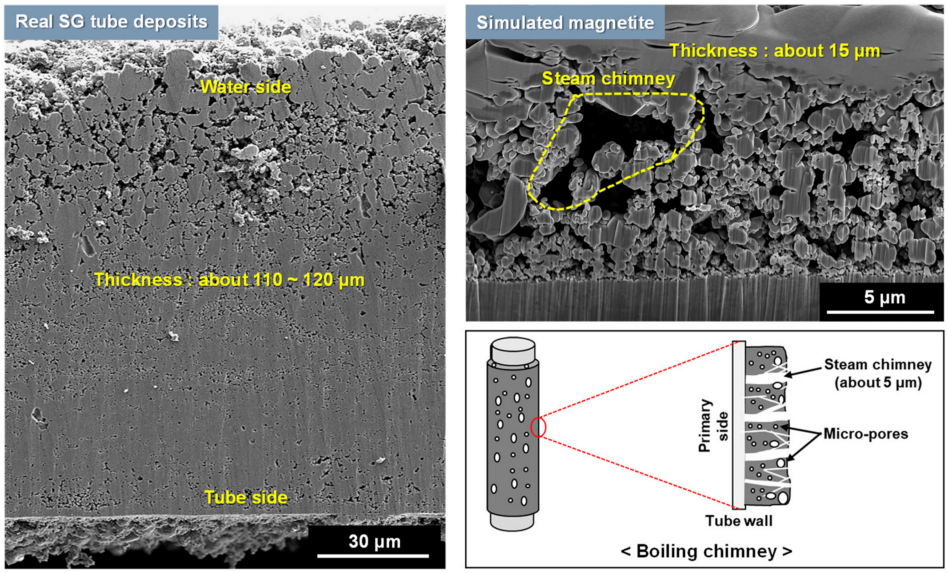

Figure 8. Cross-sectional view of the real SG tube deposits and simulated magnetite deposits.

Figure 9 presents the porosity of the simulated deposits and the flakes. The thickness of the flakes was much greater than that of the simulated deposits. Hence, the flakes were divided into the three regions by location: (1) water side, a region exposed to high temperature water; (2) tube side, a region in contact with the surface of an SG tube; and (3) middle side, an intermediate region between the water and tube sides. The porosity of the flake samples increased from the tube side to the water side. This result may be closely related with the bubble growth and steam chimneys from the tube side to the water side [23,31]. Although the porosity of the entire region of simulated deposits was quite different from that of the flake samples, the porosity of the simulated deposits was almost the same as that of the water side of the flake samples, with about 26% porosity.

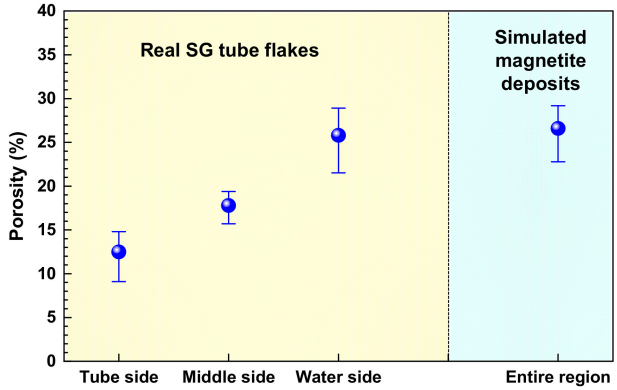

Figure 9. Porosity of the simulated deposit and real SG tube flakes.

3.2. Phases of Simulated Magnetite Deposits and Real Flake Samples

Figure 10a presents the XRD patterns of the simulated deposits. The diffraction peaks of the simulated deposits were well coincided with the XRD reference data of pure magnetite (PDF number 00-019-0629). In addition, Figure 10b shows a typical chemical composition of the simulated deposit particle using SEM-EDS analysis, which shows that the particle was identified as magnetite. The XRD and SEM-EDS data confirmed that the simulated deposit was pure magnetite, which means the deposition test well simulated the actual SG tube deposits because the actual SG tube deposits mainly consisted of magnetite (about 90~95%).

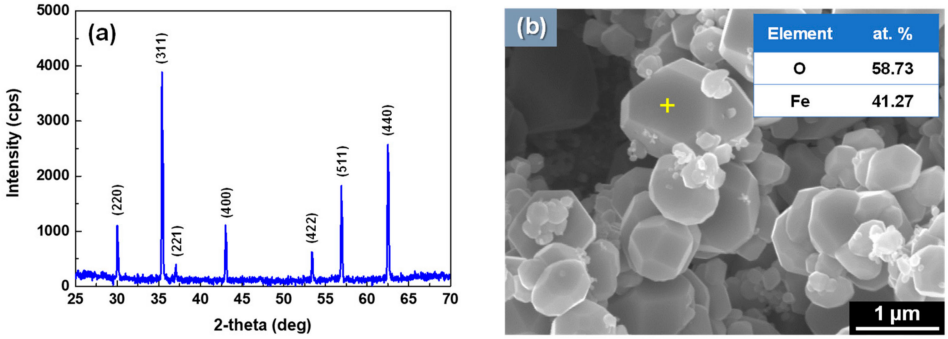

Figure 10. (**a**) X-ray diffractometer (XRD) pattern of simulated deposit and (**b**) a representative chemical composition of particle deposited in the test by SEM-energy dispersive X-ray spectrometer (EDS) analysis.

Figure 11 presents the EBSD data of the real SG tube flakes. As shown in Figure 11a, the EBSD analyzed area contained the number of the pores with a size of about 0.2~1.0 μm. Figure 11b shows the 001 inverse pole figure orientation map. A random orientation was presented in pole figure orientation map because the preferred orientation color did not appear. Figure 11c shows the EBSD phase identification map. Four phases were observed in the map as follows: magnetite (Fe_3O_4),

trevorite (Ni_2FeO_4), jacobsite (Mn_2FeO_4), and metallic Cu. Zero solutions (black regions) were also detected and randomly formed in all of the analyzed area. In these EBSD results, we believed that the micro-pores could represent the zero solutions. In general, it is well known that zero solutions are points in the scan for which no indexing solution could be found for the corresponding Kikuchi pattern [32]. Hence, except for zero solutions, the fractions of the four phases were simply normalized to 100%. The normalized phase fractions of the flake sample are presented in Figure 11d. These results showed that the SG tube flake samples were mainly composed of magnetite and consisted of small amounts of trevorite, jacobsite, and metallic Cu particle. The simulated magnetite deposits were sufficiently similar to simulate the SG flakes of actual PWRs because the real SG flakes consisted of 90% magnetite and had a porous structure. Furthermore, we conclude that the various compounds of the actual SG tube flakes could be perfectly simulated using the loop system by injecting the additional sources such as Ni, Mn, Cr, and Cu.

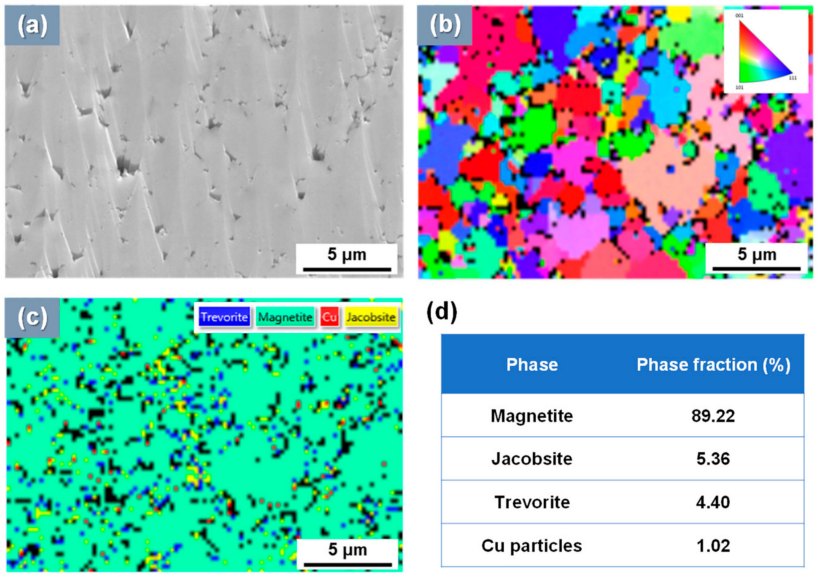

Phase	Phase fraction (%)
Magnetite	89.22
Jacobsite	5.36
Trevorite	4.40
Cu particles	1.02

Figure 11. Electron back-scatter diffraction (EBSD) data of the real SG tube flake: (**a**) SEM image, (**b**) 001 inverse pole figure orientation map, (**c**) phase distribution map, and (**d**) relative phase fractions.

We produced porous magnetite deposits on SG tubes using a loop system and compared with the real SG tube deposits using the various analysis techniques. Table 3 summarizes the comparative analysis between the simulated magnetite deposits and real SG tube flakes. On the basis of the particle characteristics and porosity results, the magnetite deposits produced using the loop system properly simulated the real SG tube deposits because the particle size, aspect ratio, and porous structure were closely similar to those of real SG deposits.

Table 3. Comparative analyses between real steam generator (SG) tube flake and simulated magnetite deposits.

Materials	Particle Characteristics			Phases (%)	Porosity (%)	Thickness of Deposits (μm)
	Mean Size (μm)	Aspect Ratio	Morphology			
Simulated magnetite	0.90	1.13	Polyhedral & round	Pure magnetite	26.6	15
SG tube flake	0.79	1.17	Polyhedral & round	Magnetite (89.2) Jacobsite (5.4) Trevorite (4.4) Copper (1.0)	18.7	110~120

3.3. Amount of Magnetite Deposits and Mechanism of Magnetite Deposition Behavior

Figure 12 presents the amount of simulated magnetite deposits per unit area deposited onto the Alloy 690TT. The average amount of the deposits was 4.97 mg/cm^2. Using the deposition loop system, the deposition rate of magnetite deposits was 0.36 mg/cm^2·day. Good reproducibility was confirmed.

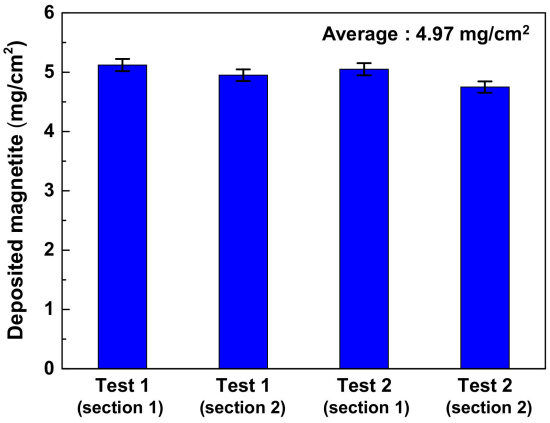

Figure 12. Amount of magnetite deposited onto Alloy 690TT tube.

The main factors affecting the deposition behavior of particles have been reported in previous works [31,33]; these include thermal hydraulic factors (temperature, pressure, heat flux, flow velocity), water chemistry factors (pH, dissolved oxygen), particle factors (size, concentration, zeta potential, solubility), and substrate factors (zeta potential, roughness). Fe solubility is an important factor to consider in magnetite deposition, which is a function of temperature and pH [34]. Under the operating conditions of PWR secondary coolant (pH value: 8.8~9.6 at 25 °C, temperature: 230~280 °C), the Fe solubility tends to decrease with the increase of coolant temperature [34]. In addition, the Fe solubility was decreased with the increase of pH from 8.8 to 9.6 at operating temperature [34]. These indicate that Fe ions easily precipitated to magnetite particles, increasing the amount of magnetite deposits. However, in this experimental condition, there is no variation of the Fe solubility because most of the variables containing the temperature and pH were continuously maintained during the deposition tests.

In this work, the magnetite deposition behavior on the Alloy 690TT tube could be explained by boiling on the tube surface and the magnetite mass is proportional to the SNB behavior. SNB occurs when the surface temperature is higher than the saturated liquid temperature and the bulk liquid temperature remains below the saturation temperature. Many PWRs are currently being operated under SNB conditions to enhance the heat transfer rate [35]. Under SNB conditions of PWRs, the magnetite deposition model on boiling heat transfer surface could be explained as following the four steps [36]: (1) once the steam bubbles grow, (2) magnetite particles suspended in the coolant are adhered to the interface between the coolant and vapor bubble, (3) the particles are transported to the micro-layer evaporation region beneath the vapor bubble, and (4) evaporation into the vapor bubble removes the coolant from the particles and they can then agglomerate to form of the deposits by Van Der Waals or electrostatic forces [36]. These repetitive processes could increase the magnetite deposition mass.

In addition, a relationship between electrostatic force and magnetite deposition was used for a better understanding of the magnetite deposition behavior on Alloy 690TT tubes. The deposition behavior of colloidal particles on a metal surface is affected by the electrostatic force between the particle and surface [33,37]. Therefore, we measured the zeta potential of the magnetite nanoparticles and surface zeta potential of Alloy 690TT in the secondary coolant.

Figure 13 shows the zeta potential of the magnetite nanoparticles and the surface zeta potential of Alloy 690TT. In the initial stage of magnetite deposition, the difference of zeta potentials between the bare surface of Alloy 690TT and magnetite particles acts as an electrostatic driving force to control

the deposition of magnetite particles. Measured zeta potentials of magnetite and Alloy 690TT surface showed all negatively charged values as −24.0 and −28.2 mV, respectively. These results indicate that the repulsive force works between the particles and the surface when the magnetite particles come close to the Alloy 690TT surface. The zeta potential differences between the magnetite nanoparticles and the Alloy 690TT surface were 4.2 mV. However, after the surface of Alloy 690 TT tube was fully covered with the first magnetite deposit layer, the zeta potential differences between the bare surface of the tube and magnetite particles might no longer affect the subsequent deposition of the second or above magnetite layer. After that, the electrostatic force between the already deposited magnetite layers and magnetite nanoparticles in the coolant would become a factor controlling the magnetite deposition behavior. In this case, the electrostatic force could be explained by the zeta potential between magnetite nanoparticles. However, the zeta potentials in this work were measured at room temperature owing to the specification limitation of the zetameter, whereas the magnetite was accumulated at 270 °C. Hence, there may be some limitations in understanding the mechanism of magnetite deposition on the surface of SG tubes. Nevertheless, considering that the surface of magnetite particles is still negatively charged at high temperatures up to 320 °C [38], it seems that the zeta potentials of the magnetite particles and Alloy 690TT surface are still effective and reliable at 270 °C, as tested in this study.

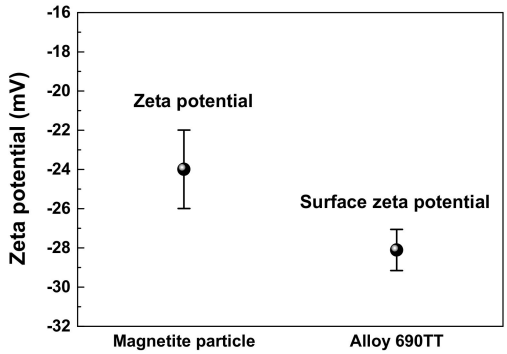

Figure 13. Zeta potentials of magnetite nanoparticle and Alloy 690TT surface.

The reaction for the magnetite formation by injecting the Fe(II)-acetate in simulated secondary coolant using the loop system can be described as follows:

$$Fe(CH_3COO)_2 + 2H_2O \rightarrow Fe(OH)_2 + 2CH_3COOH \quad (1)$$

$$3Fe(OH)_2 \rightarrow Fe_3O_4 + 2H_2O + H_2 \quad (2)$$

$$CH_3COOH + OH^- \rightarrow CH_3COO^- + H_2O \quad (3)$$

Equation (1) indicates that Fe(II)-acetate reacts with water to produce $Fe(OH)_2$ and CH_3COOH in the Fe source tank. When $Fe(OH)_2$ and CH_3COOH are injected into the test section, magnetite nanoparticles are formed from $Fe(OH)_2$ and CH_3COO^- ions occurring in the secondary coolant according to Equations (2) and (3), respectively. Vereda et al. [39] studied the specific ion effects on the electrokinetic properties of magnetite nanoparticles. They measured the electrophoretic mobility of magnetite nanoparticles in the presence of several anions taken from the representative Hofmeister series such as CH_3COO^-, $citrate^{3-}$, SO_4^{2-}, F^-, Cl^-, and NO_3^-, among others. They reported that the addition of an electrolyte lowered the electrophoretic mobility of magnetite particles owing to a decrease of the effective positive surface charge of the particles as the counter ions (anions) approach the surface of particles. Therefore, in this work, the presence of CH_3COO^- ions in the solution decreases the electrophoretic mobility of magnetite nanoparticles. A low value of electrophoretic mobility of magnetite means that the zeta potential of magnetite becomes lower according to Henry's equation.

3.4. Simulation of Chemical Impurity Concentration within the Micro-Pores of Magnetite Deposits

Many researchers have presented that aggressive chemical impurities are concentrated within the micro-pores of the SG tube deposits and tube sheet sludge owing to the evaporation of secondary water within the micro-pores [22,23]. These phenomena accelerated the corrosion rate of the SG components owing to the formation of severe corrosive environments [22,23]. Hence, the SG tube deposit specimens, which concentrated the chemical impurities, could be widely used in many investigations related to the corrosion behaviors. In particular, if the Na and Cl could be concentrated within the micro-pores of the simulated SG tube deposits, it would be used to investigate the pitting corrosion and chloride induced stress corrosion cracking. Hence, by injecting the Na and Cl ions with the Fe source during the deposition test process, we examined the concentration behavior of these impurities in the pores of magnetite deposits.

Figure 14 shows the STEM-EDS mapping analysis of Na and Cl impurities in the micro-pores formed on the tube side of the simulated magnetite deposits. The elemental maps clearly present that bulk particles consisted of Fe and O. However, as expected, Na and Cl are mainly observed on the outer surfaces of magnetite particles. As presented in Table 4, the average concentration of impurities within the micro-pores formed on the tube side of the magnetite deposits was estimated to be 4700 ppm for Na and 400 ppm for Cl by STEM-EDS point analyses. The concentration factors of impurities are defined as the ratio of impurity concentration on the pores to the concentration in the bulk water. As the concentrations of Na and Cl in the bulk solution in the test section were 0.1 ppm and 0.15 ppm, respectively, the concentration factors of Na and Cl within the deposits were evaluated to be approximately 4.7×10^5 and 2.7×10^3, respectively. In a previous study, the concentration factors of both Na and Cl within the micro-pores of real SG flakes were 4×10^4 [23]. The impurity concentration is a complex phenomenon that is affected by numerous factors; therefore, direct comparison of the concentration factors might be a difficult task. Nevertheless, it is concluded that Na and Cl impurities can be concentrated in the pores of the simulated deposits. Furthermore, we think that other impurities such as S and P ions could also be concentrated in the pore of simulated deposits using the loop system.

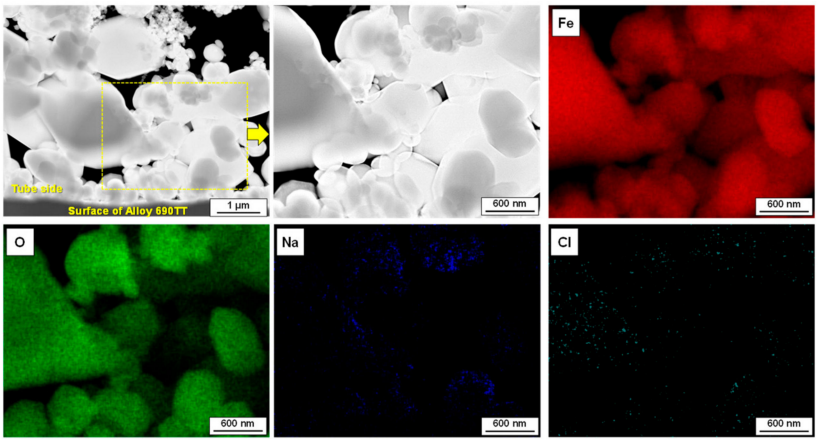

Figure 14. Transmission electron microscope (TEM)-EDS mapping analysis of the Na and Cl impurities in the micro-pores formed on the tube side of simulated magnetite deposits.

Table 4. Comparison of the concentration of impurities between both deposit samples.

Materials	Impurities (wt.%)		Bulk Water (ppb)		Concentration Factors	
	Na	Cl	Na	Cl	Na	Cl
Simulated magnetite	0.47	0.04	100	150	4.7×10^5	2.7×10^3
SG tube flake [23]	0.02	0.04	<5	<10	4.0×10^4	4.0×10^4

4. Conclusions

(1) The simulated magnetite deposits and real SG tube flakes have the round and polyhedral particles with numerous small pores. On the basis of the particle characteristics and porosity results, the magnetite deposits produced using the loop system properly simulated the real SG tube deposits because the particle size, aspect ratio, and porous structure were closely similar to those of real deposits.

(2) The simulated deposit was pure magnetite, which means the deposition test well simulated the actual SG tube deposits because the actual SG tube deposits mainly consisted of magnetite (about 90~95%). The average amount and deposition rate of simulated deposits were 4.97 mg/cm^2 and 0.36 mg/cm^2·day, respectively.

(3) Chemical impurities such as Na and Cl could be concentrated within the micro-pores of the magnetite deposits owing to the bubble formation and collapse. The concentration factors of Na and Cl within the deposits were evaluated to be approximately 4.7×10^5 and 2.7×10^3, respectively.

(4) These simulated magnetite samples would be used to investigate the heat transfer degradation of SG tubes and corrosion behavior such as the magnetite accelerated corrosion, impurities induced stress corrosion cracking, and pitting corrosion.

Author Contributions: S.-H.J. wrote the paper and analyzed the data, H.-S.S. and D.H.H. designed the experiments and revised the paper, J.-M.L. performed the experiments, J.H. performed the experiments during the revision process. All authors have read and agreed to the published version of the manuscript.

Funding: This work was supported by the National Research Foundation (NRF) grant funded by the government of the Republic of Korea (2017M2A8A4015159).

Conflicts of Interest: The authors declare no conflict of interest. The sponsor had no role in the design of the study; in the collection, analyses or interpretation of data; in the writing of the manuscript; or in the decision to publish the results.

References

1. Vepsäläinen, M.; Saario, T. *Magnetite Dissolution and Deposition in NPP Secondary Circuit*; VTT-R-09735-10; VTT Technical Research Centre of Finland: Espoo, Finland, 2010.
2. Ramesh, C.; Murugesan, N.; Prince, A.A.M.; Velmurugan, S.; Narasimhan, S.V.; Ganesan, V. Applied of polymer electrolyte based hydrogen sensor to study corrosion of carbon steel in acid medium. *Corros. Sci.* **2001**, *43*, 1865–1875. [CrossRef]
3. Prince, A.A.M.; Velmurugan, S.; Narasimhan, S.V.; Ramesh, C.; Murugesan, N.; Raghavan, P.S.; Gopalan, R.J. Dissolution behaviour of magnetite film formed over carbon steel in dilute organic acid media. *J. Nucl. Mater.* **2001**, *289*, 281–290. [CrossRef]
4. Yang, G.; Pointeau, E.; Tevissen, E.; Chagnes, A. A review on clogging of recirculating steam generators in pressurized-water reactors. *Prog. Nucl. Energy* **2017**, *97*, 182–196. [CrossRef]
5. Paine, J.P.N.; Hobart, S.A.; Sawochka, S.G. Predicting steam generator crevice chemistry. In Proceedings of the 5th International Symposium on Environmental Degradation of Materials in Nuclear Power Systems-Water Reactors, Monterey, CA, USA, 25–29 August 1991; pp. 739–744.
6. Millet, P.J.; Fenton, J.M. A detailed model of localized concentration processes in porous deposits of SGs. In Proceedings of the 5th International Symposium on Environmental Degradation of Materials in Nuclear Power Systems-Water Reactors, Monterey, CA, USA, 25–29 August 1991; pp. 745–751.
7. Plonski, I.J. Efect of bare metal surface on the dissolution in aqueous citrate solutions of magnetite films on carbon steel. *J. Appl. Electrochem.* **1997**, *27*, 1184–1192. [CrossRef]
8. Gonzalez, F.; Spekkens, P. Corrosion of Inconel 600 under steam generator sludge piles. In Proceedings of the 4th International Symposium on Environmental Degradation of Materials in Nuclear Power Systems-Water Reactors, Jekyll Island, GA, USA, 6–10 August 1989; p. 7-108–7-120.
9. Saint Paul, P.; Slama, G. Steam generator materials degradation. In Proceedings of the 5th International Symposium on Environmental Degradation of Materials in Nuclear Power Systems-Water Reactors, Monterey, CA, USA, 25–29 August 1991; pp. 39–49.

10. Kawamura, H.; Hirano, H. Intergranular attack and stress corrosion cracking propagation behavior of Inconel 600 in high temperature water. In Proceedings of the 6th International Symposium on Environmental Degradation of Materials in Nuclear Power Systems-Water Reactors, San Diego, CA, USA, 1–5 August 1993; pp. 71–78.
11. Förch, H.; Oliver, T.; Hertle, W. Chemical cleaning of PWR steam generator with a low temperature process. *Nucl. Eng. Design* **1993**, *147*, 115–118. [CrossRef]
12. Jeong, W.-T.; Hong, S.-Y. Development of the tube sheet cleaning system of the nuclear steam generator. In Proceedings of the Transactions of the Korean Nuclear Society Autumn Meeting, Busan, Korea, 27–28 October 2005.
13. Marks, C. *Steam Generator Management Program: Effects of Different pH Control Agents on Pressurized Water Reactor Plant Systems and Components*; EPRI Report 1019042; EPRI: Palo Alto, CA, USA, 2009.
14. Byers, W.A.; Deshon, J. Structure and chemistry of PWR crud. In Proceedings of the International Conference on Water Chemistry of Nuclear Reactor Systems, San Francisco, CA, USA, 11–14 October 2004; pp. 1722–1731.
15. Deshon, J. *PWR Axial Offset Anomaly (AOA) Guidelines Rev. 1*; EPRI Report 1008102; EPRI: Palo Alto, CA, USA, 2004.
16. Sawicki, J.A. *Characterization of Corrosion Products on the Callaway Cycle 9 PWR Core*; EPRI Report 1003129; EPRI: Palo Alto, CA, USA, 2001.
17. Sawicki, J.A. Evidence of Ni_2FeBO_5 and m-ZrO_2 precipitates in fuel rod deposits in a AOA-affected high boiling duty PWR core. *J. Nucl. Mater.* **2008**, *374*, 248–269. [CrossRef]
18. Nishimura, T.; Umehara, R.; Shimizu, Y.; Kogawa, N.; Ojima, Z.; Nagamine, K.; Suzuki, M. Study for nickel deposition on the fuel cladding by DH transition under simulated PWR conditions. In Proceedings of the Nuclear Plant Chemistry Conference 2014, Sapporo, Japan, 26–31 October 2014; p. 10152.
19. Baek, S.H.; Shim, H.-S.; Kim, J.G.; Hur, D.H. Effect of chemical etching of fuel cladding surface on crud deposition behavior in simulated primary water of PWRs at 328 °C. *Ann. Nucl. Energy* **2018**, *116*, 69–77. [CrossRef]
20. Baek, S.H.; Shim, H.-S.; Kim, J.G.; Hur, D.H. Effects of heat flux on fuel crud deposition and sub-cooled nucleate boiling in simulated PWR primary water at 13 MPa. *Ann. Nucl. Energy* **2019**, *133*, 178–185. [CrossRef]
21. Baek, S.H.; Shim, H.-S.; Kim, J.G.; Hur, D.H. Effect of dissolved hydrogen on fuel crud deposition and subcooled nucleate boiling in PWR primary water at 328 °C. *Nucl. Eng. Des.* **2019**, *345*, 85–93. [CrossRef]
22. Jeon, S.-H.; Song, G.D.; Hur, D.H. Micro-Galvanic Corrosion of Steam Generator Materials within Pores of Magnetite Flakes in Alkaline Solutions. *Metals* **2018**, *8*, 899. [CrossRef]
23. Jeon, S.-H.; Hong, S.; Kwon, H.C.; Hur, D.H. Characteristics of steam generator tube deposits in an operating pressurized water reactor. *J. Nucl. Mater.* **2018**, *507*, 371–380. [CrossRef]
24. Goujon, C.; Bescond, A.; Mansour, C.; Delaunay, S.; Pauporté, T.; Bretelle, J.-L. Fouling Of Steam Generator Tubes In Nuclear Power Plants: Laboratory Tests To Reproduce Oxides Deposition And Chemical Cleanings. Nuclear Plant. In Proceedings of the Chemistry Conference 2014, Sapporo, Japan, 26–31 October 2014; p. 10098.
25. Fruzzetti, K. *Pressurized Water Reactor Secondary Water Chemistry Guidelines-Revision 8*; EPRI Report 3002010645; EPRI: Palo Alto, CA, USA, 2017.
26. Vijayakumar, R.; Koltypin, Y.; Felner, I.; Gedanken, A. Sonochemical synthesis and characterization of pure nanometer-sized Fe_3O_4 particles. *Mater. Sci. Eng. A.* **2000**, *286*, 101–105. [CrossRef]
27. Gotić, M.; Musić, S. Synthesis of nanocrystalline iron oxide particles in the iron(III) acetate/alcohol/acetic acid system. *Eur. J. Inorg. Chem.* **2008**, 966–973. [CrossRef]
28. Chirita, M.; Banica, R.; Sfirloaga, P.; Ieta, A.; Grozescu, I. A short route of micrometric magnetite synthesis via Fe-EDTA thermal decomposition. In Proceedings of the International Semiconductor Conference, Sinaia, Romania, 11–13 October 2010.
29. Chen, L.; Zhao, C.; Zhou, Y.; Peng, H.; Zheng, Y. Controlled synthesis of Fe_3O_4 nanosheets via one-step pyrolysis of EDTA ferric sodium salt. *J. Alloys Compd.* **2010**, *504*, L46–L50. [CrossRef]
30. Kim, K.-S.; Baek, S.H.; Shim, H.-S.; Lee, J.H.; Hur, D.H. Effect of zinc addition on fuel crud deposition on simulated PWR primary coolant conditions. *Ann. Nucl. Energy* **2020**, *146*, 107643. [CrossRef]
31. Mclean, V. *Characterization of PWR Steam Generator Deposits*; EPRI TR-106048; EPRI: Palo Alto, CA, USA, 1996.

32. Wright, S.I.; Nowell, M.M.; Lindeman, S.P.; Camus, P.P.; Graef, M.D.; Jackson, M.A. Introduction and comparison of new EBSD post-processing methodologies. *Ultramicroscopy* **2015**, *159*, 81–94. [CrossRef] [PubMed]
33. Fruzzetti, K. *Multivariable Assessment of Flow Accelerated Corrosion and Steam Generator Fouling, Literature Review*; EPRI Report 1003619; EPRI: Palo Alto, CA, USA, 2003.
34. Dooley, R.B. Flow-accelerated corrosion in fossil and combined cycle/HRSG plants. *Powerpl. Chem.* **2008**, *10*, 68–89.
35. Guzzetta, A. Modelling the effects of fuel rod crud formation on boiling heat transfer in a pressurized water reactor using eulerian two-fluid CFD. Master's Thesis, Pennsylvania State University, University Park, PA, USA, 2010.
36. Iwahori, T.; Mizuni, T.; Koyama, H. Role of surface chemistry in crud deposition on heat transfer surface. *Corrosion* **1979**, *35*, 345–350. [CrossRef]
37. Essi, J.; Konsta, S.; Timo, S. Determining zeta potential of magnetite particles in PWR secondary side water treated with ammonia or ethanolamine by using streaming potential technique. In Proceedings of the 20th NPC International Conference, Brighton, UK, 2–7 October 2016. Paper Number 151.
38. Vidojkovic, S.M.; Rakin, M.P. Surface properties of magnetite in high temperature aqueous electrolyte solutions: A. review. *Adv. Colloid Interface Sci.* **2017**, *245*, 108–129. [CrossRef] [PubMed]
39. Vereda, F.; Molina, A.M.; Alvarez, R.H.; Pérez, M.Q. Specific ion effects on the electrokinetic properties of iron oxide nanoparticles: Experiments and simulations. *Phys. Chem. Chem. Phys.* **2015**, *17*, 17069–17078. [CrossRef] [PubMed]